

Cite this: *Mater. Adv.*, 2024,
5, 5595

Ab initio insight into furan conversion to levulinate ester in reaction with methylal and methanol†

Yun-Sim Kim, Ryong-Wan Ham, Yong-Chol Pak, Man-Sok O and Chol-Jun Yu *

Recently, methyl levulinate (MLA) has attracted remarkable attention as a promising fuel additive and its synthesis route from furan and dimethoxymethane (DMM or methylal) has been exploited, but the reaction pathway remains indistinct. In this work, we study the conversion of furan into MLA in reaction with DMM and methanol using *ab initio* calculations with double- ζ polarization basis sets plus supercell method and B3LYP/6-311+G* basis sets plus cluster method. Our calculations reveal that the reaction of furan + DMM to 2-methoxymethyl-furan (MMF) + methanol is endothermic in vacuum but exothermic in methanol solvent, while the reaction of MMF + water to MLA is exothermic both in vacuum and methanol solvent environments. Moreover, we identify the reaction sites of the individual reactant molecules by analyzing their Fukui functions and verify the Brønsted acid–base reaction fashions for these reactions. Finally, we determine the activation energies for the reactions without and with a protonated methanol molecule, together with the detailed geometries of the intermediates.

Received 3rd May 2024,
Accepted 26th May 2024

DOI: 10.1039/d4ma00446a

rsc.li/materials-advances

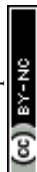
1 Introduction

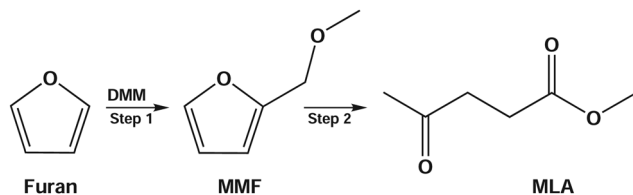
Due to dwindling fossil reserves and increasing environmental concerns, the extensive search and efficient utilization of renewable resources have drawn enormous attention.^{1,2} Deriving from plant photosynthesis, biomass is a promising source of cheap and renewable energy, and has been widely used for producing high value-added bio-fuels and chemicals.^{3–5} Recently, a significant research interest has been focused on efficient conversion of biomass or biomass-derived educts into value-added chemicals such as 5-hydroxymethylfurfural (HMF),^{6–9} levulinic acid (LA),^{10,11} and levulinate esters.^{12,13} Among them, levulinate esters including alkyl (methyl, ethyl, propyl, butyl) levulinates are particularly important due to their wide applications in medicine, flavoring and fragrance industries as well as their use as fuel additives for improving properties of petroleum and diesel.¹⁴

Alkyl levulinates can be produced from various biomass-derived products such as sugars (glucose,^{13,15} fructose,¹² xylose¹⁶), cellulose,^{1,17} furfural,^{16,18} furfuryl alcohol,¹⁹ furan,²⁰ and raw biomass itself.^{21–23} The direct synthesis of methyl levulinate (MLA) from sugars or cellulose has shown the problems of low yield and very demanding conditions. For example, the one-pot conversion of xylose to MLA with the co-catalysts of Pd/Al₂O₃ and amberlyst at 7.0 MPa H₂ pressure had a yield of 25%.²⁴ Hu *et al.*¹⁶ have reported 52.5 and 37.7% yields of MLA from glucose and xylose at 160 °C. On the other hand, the furfural and furfuryl alcohol are commercially produced from sugars with a high cost of industrial production due to the complicated purification and separation processes. To address these drawbacks, some works reported the synthesis of MLA from furan, which is an important product by catalytic pyrolysis of biomass and used for producing value-added chemical of tetrahydrofuran.^{25,26} However, the acid-catalyzed conversion of furan has produced benzofuran but not MLA or levulinic acid.²⁷ The structural difference between furfuryl alcohol and furan is the additional hydroxymethyl group in furfuryl alcohol. To solve the problem, Zhang *et al.*²⁰ developed a new reaction route to produce MLA, in which furan reacts with dimethoxymethane (DMM or methylal) to form 2-methoxymethyl-furan (MMF) as the reactive intermediate and then MMF was converted to MLA *via* acid catalysis with a co-solvent/reactant of methanol (see Scheme 1). Using the acid-catalyzed conversion to MLA in DMM/methanol solvent, they achieved a higher yield of 67.9% at 170 °C from furan. In this reaction, DMM is the

Computational Materials Design, Faculty of Materials Science, Kim Il Sung University, Ryongnam-Dong, Taesong District, Pyongyang, People's Republic of Korea. E-mail: cj.yu@ryongnamsan.edu.kp

† Electronic supplementary information (ESI) available: Tables for bond lengths, bond angles and dipole moment of MMF, MLA, methanol and water molecules, for Fukui indices of molecules and for DFT total energies of reactants and products, and figures for temperature fluctuation during AIMD equilibration, configurations of 26 and 41 methanol molecules, isodensity surface of Fukui functions in methanol and water, and detailed geometries of intermediates during NEB runs. See DOI: <https://doi.org/10.1039/d4ma00446a>





Scheme 1 Reaction pathway for producing methyl levulinate (MLA) from furan in DMM/methanol medium.²⁰

most important reactant that enables furan to convert into MLA. As the smallest member of oxygenated methyl ethers, which are attractive additives for diesel fuels,^{28–30} DMM itself has been used as a fuel and can be produced from biomass and feedstock.

To understand the reaction mechanism of furan conversion to MLA in reaction with DMM/methanol, *ab initio* study based on quantum theory such as density functional theory (DFT) or Hartree–Fock (HF) theory is necessary. For furan, many theoretical works have been reported for its structural and vibrational properties^{31,32} and reactivity with small molecules.^{33,34} For the case of DMM, we found the *ab initio* works for the different conformations³⁵ and the pyrolysis/combustion.^{36,37} The conformational equilibrium of the alkyl levulinates has been studied by using the force field method (MMFF94),³⁸ and the thermochemical studies of levulinic acid esters have been performed.^{39,40} However, no theoretical work for furan conversion to MLA is yet performed, remaining its atomistic understanding indistinct.

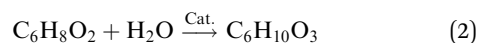
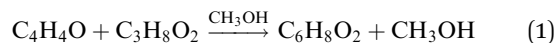
In this work, we performed *ab initio* calculations within the DFT framework to get an atomistic insight into the reaction pathway of furan conversion to MLA. The supercell and cluster modelings were used for the isolated molecules of furan, DMM, MMF and MLA. The solvent effect was considered explicitly by including certain numbers of solvent (methanol) molecules in the supercell and implicitly by using the conductor-like screening model (COSMO). The reaction energies and activation barriers were estimated, together with the detailed structures of intermediates. In the following, Section 2 describes the computational methods, Section 3 explains the results, and Section 4 gives the conclusions.

2 Computational methods

2.1 Supercell and cluster modeling

In this work, we made modeling of isolated molecules using both supercell and cluster models to have confidence in the calculation. For the supercell models, we constructed the three-dimensional (3D) periodic cubic supercells with a lattice constant of 30 Å, which can provide a long distance enough for artificial interaction between the periodic molecular images to be negligible. The isolated molecules in this work include furan (C₄H₄O), DMM (C₃H₈O), methanol (CH₃OH), MMF (C₆H₈O₂), water (H₂O) and MLA (C₆H₁₀O₃). In fact, according to the reaction route for furan conversion to MLA developed by Zhang

et al.,²⁰ the chemical reactions can be expressed as follows,



where Cat. is the solid acidic resin catalyst. To consider the effect of methanol solvent on the molecular structures and reaction energetics, we explicitly included certain numbers of methanol molecules in the supercells in view of methanol density of 0.791 g cm⁻³; 25 molecules in the supercell with a lattice constant of 12 Å and 40 molecules in the 14 Å supercell. The reason for using the different numbers of molecules is to give an estimation of supercell size effect on the results.

For the cluster modeling, which is more appropriate for molecules with higher accuracy and lower computational cost than the supercell modeling, there is no need to use the 3D periodic supercell. The solvent effect was implicitly considered by using COSMO approach⁴¹ with the experimental value of dielectric constant of methanol (32.6⁴²).

2.2 Pseudopotential PAO calculations for supercell models

For the supercell models, we applied the pseudopotential and pseudo atomic orbital (PAO) basis sets method as implemented in the SIESTA (version 4.1) package.⁴³ For the electrostatic interaction between the ionic cores and valence electrons, we constructed the non-relativistic Troullier–Martins-type norm-conserving pseudopotentials⁴⁴ by using the ATOM code provided in the package with the valence configurations of C-2s²2p², O-2s²2p⁴ and H-1s¹. For the exchange–correlation (XC) interaction between the valence electrons, we tested different types of functionals such as Perdew–Zunger (PZ) formalism within the local density approximation (LDA)⁴⁵ and Perdew–Burke–Ernzerhof (PBE) formalism⁴⁶ and Becke–Lee–Yang–Parr (BLYP)^{47,48} formalism within the generalized gradient approximation (GGA). To take into account the van der Waals (vdW) interaction, which is important in molecules, we adopted the semi-empirical approach developed by Grimme.⁴⁹ For PAOs, we used the standard double- ζ plus polarization (DZP) basis sets for all the atoms, generated with an energy shift of 300 meV for orbital-confining cutoff radii and a split norm of 0.25 for split valence of basis. All the calculations were carried out with the plane-wave cutoff energy of 300 Ry and only Γ -point in the first Brillouin zone. All the atoms were relaxed until the forces on atoms became less than 0.01 eV Å⁻¹.

For an isolated molecule in vacuum, the lowest energy conformation was derived by performing the conformational search, in which the stochastic search approach was adopted. The molecular structures of the resultant conformations were then optimized using the conjugate gradient (CG) method. To get the equilibrium states for the explicit methanol-solvent models, we performed *ab initio* molecular dynamics (AIMD) simulations at room temperature (300 K) controlled by means of a Nosé thermostat, a time step of 1 fs and duration of 1 ps. Then, the resultant structures were re-optimized using the CG method.



The activation energies were estimated for the chemical reactions described by eqn (1) and (2). To this end, we simulated the two-molecular systems of furan + DMM, MMF + methanol and MLA + water. For the reaction (1), the two-molecular systems of furan + DMM and MMF + methanol included in the supercells with vacuum (lattice constant 30 Å) and 25 and 40 methanol molecules (lattice constants 12, 14 Å) were optimized, whereas only the vacuum supercell was used for the reaction (2). To calculate the activation energy with the acceptable reaction pathway, the nudged elastic band (NEB) method⁵⁰ was applied by using our own python script in connection with the SIESTA package, as employed in our previous works.^{51–53} The number of NEB images was set to be 11 or 15. During the NEB run, all the atomic positions were relaxed and the convergence threshold was set to be 0.05 eV Å⁻¹.

2.3 All-electron AO calculations for cluster models

For the cluster models, we adopted the all-electron Gaussian-type atomic orbital (AO) method as implemented in the NWChem (version 6.6) package.⁵⁴ The geometry optimizations and frequency calculations of all the reactants, products and transition states (TS) were performed with the B3LYP^{48,55}/6-311+G* level. Different basis sets of cc-pVTZ and XC functionals of M06-2X⁵⁶ and PBE were also tested in the geometry optimization of furan. The zero-point correction (ZPC) and thermal correction (TC) to the total energy were considered. The methanol solvent effect was considered implicitly by applying the COSMO method with usage of refinement and parametrization of COSMO for real solvent (COSMO-RS)⁵⁷ and the experimental dielectric constant of methanol (32.6) as implemented in the NWChem package. In the geometry optimizations, we used the DRIVER module, which is based on the algorithm of quasi-Newton optimization with line searches and approximate energy Hessian updates. Here, the convergence criteria was set to be “tight”, which can provide the highest accuracy for geometry optimization among the possible selections in the package. The activation energies and reaction pathways were also estimated by using the NEB method with 10 beads, which was continued by running the zero-temperature string calculation with 10 beads.

3 Results and discussion

3.1 Assessment of XC functionals

Firstly, the geometry of furan was optimized using different XC functionals and basis sets with supercell and cluster modelings. Table 1 shows the bond lengths, bond angles and dipole moment of furan determined in this work. In the PAO-DZP calculations with SIESTA for the supercell models, the PZ, BLYP and PBE functionals were tested using the cubic supercell with a lattice constant of 30 Å, which contained only one furan molecule. It was found that the PZ functional within LDA underestimated the C–O bond length with a relative error of –0.19% but overestimated the C–H bond length with a relative error of 0.32%, when compared with the experimental values.⁵⁸ On the contrary, the BLYP and PBE functionals within GGA

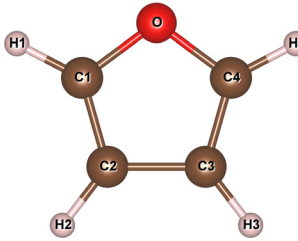
overestimated the C–O bond length with relative errors of 0.93% and 0.32% while underestimated the C–H bond length with relative errors of –0.46% and –0.07%, respectively. For the C–C bond lengths, the three XC functionals gave the underestimation compared with the experimental value.⁵⁸ On the whole, the PBE functional can be regarded to give the most reasonable geometry of furan. Therefore, we used the PBE functional for further supercell calculations.

To consider the solvent effect, we treated the supercells containing 25 and 40 methanol molecules with lattice constants of 12 and 14 Å, respectively, giving the mass densities close to the experimental value of 0.791 g cm⁻³. These molecular systems were denoted as Met-25 and Met-40. We kept a cavity with certain size around the centre of supercells to include the solute molecule later. The molecular systems were equilibrated at 300 K by performing AIMD NVT simulations during 1 ps with a time step of 1 fs and then optimized by performing atomic relaxations. Then, one furan molecule was included into the cavity of the supercells and the furan plus methanol molecular systems were again equilibrated at 300 K using 1 ps AIMD NVT simulations (see Fig. S1, ESI†). After the equilibrations, the resultant molecular systems were optimized by performing atomic relaxations with the PBE XC functional. Fig. 1 shows the obtained configurations of Met-25 and Met-40 systems without and with a furan molecule. Table 1 lists the optimized bond lengths and bond angles of furan. The bond lengths were found to be enlarged by interaction with methanol solvent molecules compared with those in vacuum.

In the AO calculations with cluster modeling, we tested two different XC functionals, such as B3LYP hybrid functional and M06-2X, and two different basis sets, such as Gaussian-type 6-311+G* and numerical cc-pVTZ. The methanol solvent effect was considered implicitly using the COSMO approach. As listed in Table 1, the B3LYP/6-311+G* method gave more reasonable bond lengths and bond angles of furan than the M06-2X/cc-pVTZ method. Our results obtained with the B3LYP/6-311+G* method were well agreed with the previous DFT works employing the UB3LYP/6-311+G* method³¹ and MP2/cc-pVTZ method.³² Therefore, we chose the B3LYP/6-311+G* method for further calculations, although some reports indicated that B3LYP was less reasonable than M06-2X for dispersion interactions.⁵⁹ When including the solvent effect, the bond lengths were also found to be slightly enlarged for both methods, being similar to the supercell calculations mentioned above. For the dipole moment, the B3LYP/6-311+G* level gave the overestimated value of 0.76 D, while the M06-2X/cc-pVTZ level yielded the underestimated value of 0.59 D, compared with the experimental value of 0.66 D. Again, the dipole moment was found to be enlarged when including the solvent effect. In addition, the PBE/6-311+G* method was found to produce relatively larger bond lengths than the experimental values (see Table S3, ESI†). We also calculated the frontier molecular orbitals of furan, such as the highest occupied molecular orbital (HOMO) and the lowest unoccupied molecular orbital (LUMO), which were –6.50 and –0.12 eV respectively (see Fig. S2, ESI†). Accordingly, the HOMO–LUMO gap was found to be 6.38 eV in good agreement with the previous DFT calculations of 6.37 eV with



Table 1 The equilibrium geometry such as bond length (unit: Å) and bond angle (unit: degree) and dipole moment (unit: Debye) for furan calculated using different methods in comparison with experiment (Exp.).⁵⁰ In the PAO-DZP supercell calculations, Met-25 and Met-40 denote the supercell calculations with the inclusion of 25 and 40 methanol solvent molecules, respectively. In the AO cluster calculations, Vac. and Met. mean the vacuum and methanol solvent environments, respectively. The right panel shows the molecular structure of furan optimized with B3LYP/6-311+G* method

| | PAO-DZP | | | | B3LYP/6-311+G* | | M06-2X/cc-PVTZ | | | Molecular structure | |
|-----------------------|---------|-------|-------|--------|----------------|-------|----------------|-------|-------|---------------------|---|
| | PZ | BLYP | PBE | Met-25 | Met-40 | Vac. | Met. | Vac. | Met. | | Exp. ^a |
| Bond length (Å) | | | | | | | | | | | |
| O–C1 | 1.359 | 1.375 | 1.366 | 1.376 | 1.372 | 1.363 | 1.368 | 1.352 | 1.357 | 1.362 |  |
| C1–C2 | 1.355 | 1.354 | 1.354 | 1.360 | 1.360 | 1.358 | 1.359 | 1.351 | 1.352 | 1.361 | |
| C2–C3 | 1.410 | 1.418 | 1.414 | 1.433 | 1.426 | 1.436 | 1.439 | 1.432 | 1.436 | 1.431 | |
| C1–H1 | 1.078 | 1.070 | 1.074 | 1.082 | 1.081 | 1.078 | 1.078 | 1.075 | 1.076 | 1.075 | |
| C2–H2 | 1.076 | 1.069 | 1.071 | 1.086 | 1.083 | 1.080 | 1.080 | 1.075 | 1.076 | 1.077 | |
| Bond angle (degree) | | | | | | | | | | | |
| C1–O–C1 | 105.5 | 105.2 | 105.4 | 106.7 | 107.7 | 106.9 | 107.0 | 107.0 | 107.2 | 106.7 | |
| C1–C2–C3 | 106.2 | 106.5 | 106.3 | 106.5 | 106.3 | 106.1 | 106.3 | 105.9 | 106.1 | 106.0 | |
| O–C1–C2 | 111.1 | 110.9 | 111.0 | 110.1 | 110.9 | 110.4 | 110.2 | 110.6 | 110.4 | 110.7 | |
| O–C1–H1 | 121.0 | 120.4 | 120.7 | 116.9 | 119.1 | 115.7 | 115.8 | 116.1 | 116.1 | 115.9 | |
| C1–C2–H2 | 124.5 | 124.3 | 124.4 | 123.4 | 123.7 | 126.5 | 126.3 | 126.5 | 126.3 | 126.1 | |
| Dipole moment (Debye) | | | | | | | | | | | |
| | | | | 0.76 | | | 0.59 | | 0.66 | | |

^a Ref. 50.

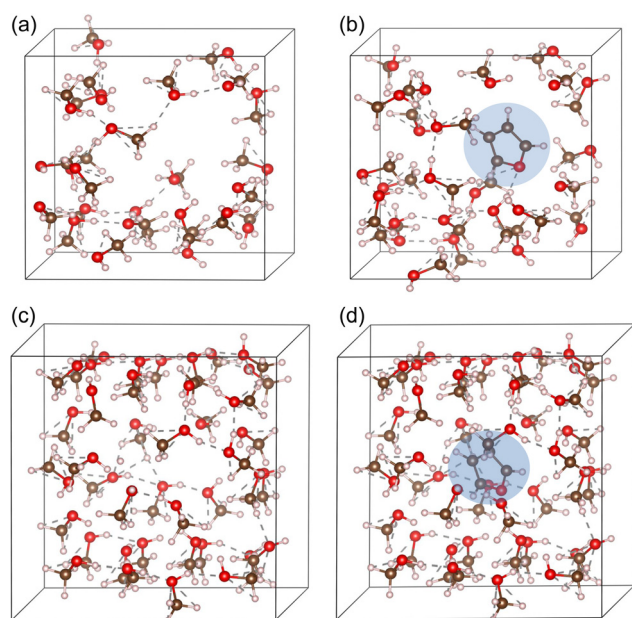


Fig. 1 Configurations of (a) 25 methanol molecules and (b) 25 methanol plus one furan molecules included in the 12 Å supercell, and (c) 40 methanol molecules and (d) 40 methanol plus one furan molecules included in the 14 Å supercell, obtained by 1 ps NVT equilibration in AIMD and subsequently atomic relaxation using the PBE functional. Dashed lines indicate hydrogen bond and blue circles show the furan molecule.

B3LYP/6-311G(2d,p)⁶⁰ and 6.00 eV with B3LYP/TZVPP.⁶¹ We calculated the harmonic frequencies of furan in good agreement with the previous calculation and experiment (see Fig. S8, ESI[†]). No imaginary frequencies were obtained, indicating that the optimized geometry (see Fig. S10, ESI[†]) is acceptable.

3.2 Geometrical features

Then, we optimized the geometries of other relevant molecules under study, such as DMM, MMF, MLA, methanol and water,

using the PBE functional for the supercell models and B3LYP/6-311+G* method for the cluster models. For the case of DMM, among several conformations including TT, TG and GG (T and G mean *trans* and *gauche*), the GG conformation was found to have the lowest energy.³⁵ Therefore, the GG conformation was used for DMM molecule in this work. Fig. 2 shows the optimized geometry of DMM in GG conformation and the HOMO and LUMO calculated with B3LYP/6-311+G*. The HOMO–LUMO gap was calculated to be 7.81 eV (see Fig. 2(b)). The bond lengths and bond angles of DMM calculated with different methods are listed in Table 2.

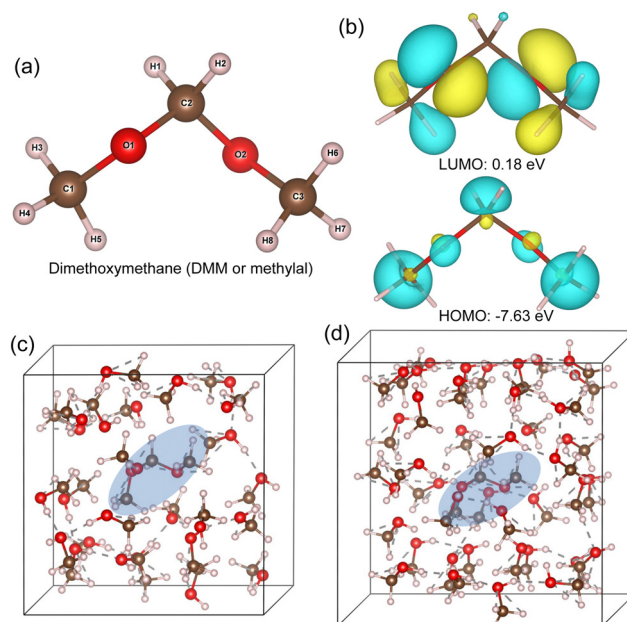


Fig. 2 (a) Geometry of DMM with a GG conformation, (b) frontier molecular orbitals including HOMO and LUMO, and configurations of (c) 25 methanol plus one DMM molecules and (d) 40 methanol plus one DMM molecules included in the 12 and 14 Å supercells, respectively.



For all the methods, the C1–O1 and C3–O2 bond lengths at the edge were found to be larger than the C2–O1 and C2–O2 bond lengths at the centre of DMM, in agreement with the previous calculation.³⁵ This can be attributed to the $n-\sigma_{\text{CO}}^*$ anomeric interaction for the interior C–O bond, originated from the delocalization of oxygen lone pair into a low lying anti-bonding σ_{CO}^* orbital.³⁵ For the PBE/DZP calculations, the inclusion of solvent methanol molecules into the supercell (Met-25 and Met-40) was found to symmetrize the molecular structure around the C2 central carbon atom, like the B3LYP/6-311+G* cluster calculations. Also, the C–O bond lengths were enlarged when considering the solvent effect implicitly for the cluster calculations.

For the MMF and MLA molecules, we performed the conformational searches to find their lowest energy conformations by applying the stochastic search algorithm that uses random generation of conformational parameters. Then, geometry optimizations were performed for the vacuum supercell models and the cluster models. For the explicit methanol solvent supercell models, the NVT equilibrations at 300 K and subsequent optimizations were performed as well. Fig. 3 shows the results for MMF and MLA (see Tables S1 and S2 for their bond lengths, bond angles and dipole moments, ESI†). The HOMO–LUMO gaps were found to be 6.08 and 6.14 eV for MMF and MLA, respectively, with the B3LYP/6-311+G* calculations. The dipole moments were calculated to be 1.29 and 1.27 D for MMF, and 5.68 and 6.51 D for MLA, in vacuum and methanol solvent environments, respectively. We also calculated the harmonic frequencies of DMM, MMF and MLA, confirming no imaginary

frequencies (see Fig. S9 and S10, ESI†). For the methanol and water molecules, the same procedure was carried out (see Fig. S3 and Tables S3, S4, ESI†).

In order to identify the reactivity species in the individual molecules, we calculated the Fukui functions describing the sensitivity of charge density with respect to the electron loss or gain. The B3LYP/6-311+G* method was used for this aim, together with the cluster models in vacuum. Fig. 4 depicts the isodensity surface view of Fukui functions mapped on the isosurface of total electron density at the value of $0.2|e| \text{ \AA}^{-3}$, representing the chemical reactivity sites with respect to electrophilic and nucleophilic attacks for the major reactant molecules of furan, DMM and MMF (see Fig. S4 for methanol and water molecules, ESI†). According to the Fukui theory, an electrophile (nucleophile) accepts (donates) a pair of electrons, forming a new chemical bond. In the case of furan, the C atoms bonded to oxygen atom (C1 and C4) were found to be reactive species as their Fukui indices for electrophilic and nucleophilic attacks had the greatest values (0.204 and 0.226 for C1 atom) among the atoms (see Table S6, ESI†). The Fukui indices for electrophilic attack (f^-) of C2 were obtained to be 0.10 and 0.13 from the Mulliken and Hirshfeld population analysis, being close to the value of 0.14 in the previous work.⁶² For the case of DMM, the O2 atom has the greatest value of Fukui index for electrophilic attack (0.215) among the atoms and the C2 central carbon atom has the higher value than those of the edge carbon atoms, indicating that the O2 and C2 atoms should be reactive species. In the MMF molecule, the carbon atoms of the furan heterocycle (C1–C4 atoms) show larger Fukui indices than the branch carbon atoms (C5 and C6 atoms), and the C6 atom of the methyl group has the negative Fukui index, indicating that the main reaction should occur in the furan heterocycle.

Table 2 The optimized bond lengths (unit: Å), bond angles (unit: degree), and dipole moment (μ) of DMM in comparison with the previous (Prev.) calculation.³⁵ Denotation of atoms is referred to Fig. 2(a)

| | PBE/DZP | | | B3LYP/6-311+G* | | Prev. ^a |
|-----------|---------|--------|--------|----------------|-------|--------------------|
| | Vac. | Met-25 | Met-40 | Vac. | Met. | Vac. |
| C1–O1 | 1.433 | 1.439 | 1.430 | 1.423 | 1.431 | 1.426 |
| C2–O1 | 1.410 | 1.402 | 1.416 | 1.404 | 1.409 | 1.406 |
| C2–O2 | 1.413 | 1.402 | 1.417 | 1.404 | 1.409 | 1.407 |
| C3–O2 | 1.428 | 1.439 | 1.429 | 1.423 | 1.431 | 1.426 |
| C1–H3 | 1.138 | 1.094 | 1.126 | 1.098 | 1.096 | 1.100 |
| C1–H4 | 1.129 | 1.094 | 1.107 | 1.094 | 1.093 | 1.096 |
| C1–H5 | 1.112 | 1.093 | 1.109 | 1.089 | 1.089 | 1.092 |
| C2–H1 | 1.116 | 1.097 | 1.111 | 1.096 | 1.094 | 1.098 |
| C2–H2 | 1.123 | 1.118 | 1.108 | 1.096 | 1.094 | 1.098 |
| C3–H6 | 1.111 | 1.103 | 1.156 | 1.098 | 1.096 | 1.100 |
| C3–H7 | 1.098 | 1.088 | 1.101 | 1.089 | 1.089 | 1.092 |
| C3–H8 | 1.114 | 1.104 | 1.127 | 1.094 | 1.093 | 1.096 |
| C1–O1–C2 | 112.0 | 111.7 | 111.3 | 113.9 | 114.0 | 113.9 |
| O1–C2–O2 | 111.8 | 113.2 | 112.6 | 114.1 | 113.8 | 114.1 |
| C3–O2–C2 | 111.3 | 110.9 | 110.1 | 113.9 | 114.0 | 113.9 |
| H1–C2–O2 | 107.5 | 107.3 | 107.5 | 105.2 | 105.6 | 105.2 |
| H2–C2–O2 | 110.2 | 107.0 | 107.0 | 110.9 | 110.5 | 110.9 |
| H6–C3–O2 | 109.6 | 108.4 | 111.9 | 110.8 | 110.5 | 110.8 |
| H7–C3–O2 | 109.7 | 104.7 | 107.0 | 106.7 | 106.8 | 106.6 |
| H8–C3–O2 | 111.8 | 114.7 | 112.9 | 111.6 | 111.4 | 111.6 |
| H3–C1–O1 | 108.7 | 110.4 | 109.6 | 110.8 | 110.5 | 110.8 |
| H4–C1–O1 | 111.6 | 111.0 | 111.3 | 111.6 | 111.4 | 111.6 |
| H5–C1–O1 | 106.9 | 107.8 | 109.1 | 106.7 | 106.8 | 106.6 |
| μ (D) | | | | 0.22 | 0.16 | 0.26 |

^a B3LYP/6-311+G** calculation.³⁵

3.3 Reaction energetics

We then calculated the DFT total energies of the relevant reactant and product molecules under study in this work to evaluate the reaction energies (see Table S7, ESI†). Table 3 lists the reaction energies evaluated by the total energy differences between the reactant and product molecules with different modelings and simulation methods. For the reaction (1), the reaction energy was calculated to be positive in vacuum as being 0.22 and 0.02 eV with PBE/DZP supercell and B3LYP/6-311+G* cluster methods, indicating that the reaction is endothermic in vacuum. However, when considering the methanol solvent effect either explicitly or implicitly, the reaction became exothermic as the reaction energies became negative both in the explicit supercell and implicit cluster calculations. In the supercell calculations, the reaction energy with Met-40 models (–0.04 eV) was found to be smaller in magnitude than that with Met-25 models (–0.28 eV). This is possibly due to the stronger interaction between the neighbouring furan molecules at the shorter distance (12 Å) in the latter case. We note that the value of –0.04 eV in the Met-40 case is close to the value of –0.07 eV obtained by cluster calculations without zero-point and thermal corrections, implying that the explicit method with the 40 methanol molecules might give



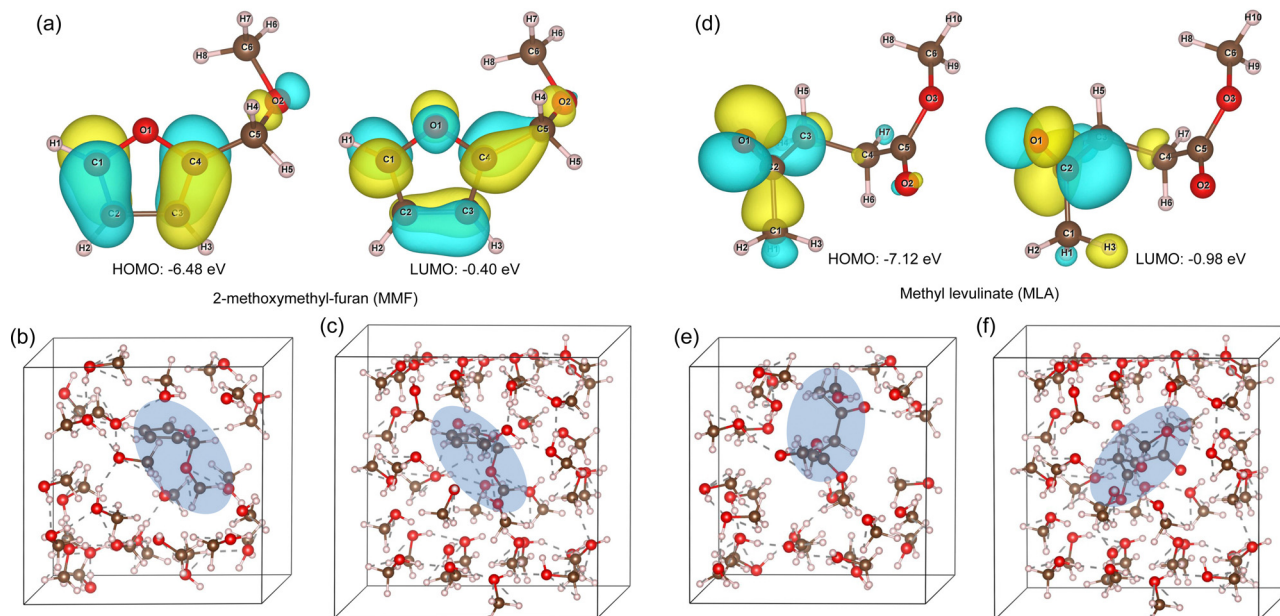


Fig. 3 Optimized geometry with HOMO and LUMO calculated with B3LYP/6-311+G* method for (a) MMF and (b) MLA, and configurations of 25 methanol molecules plus one (b) MMF and (e) MLA molecule in the 12 Å supercell and 40 methanol molecules plus one (c) MMF and (f) MLA molecule in the 14 Å supercell, equilibrated at 300 K and optimized with PBE/DZP method.

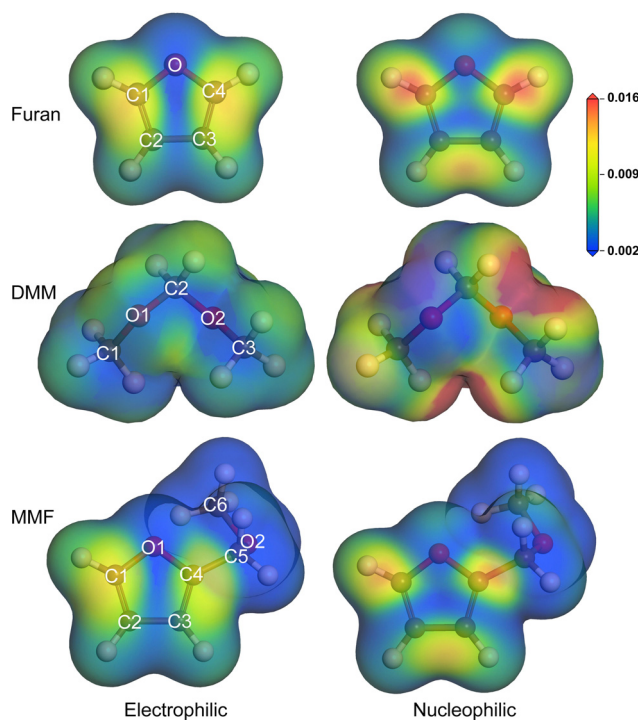


Fig. 4 Isodensity surface view of Fukui functions depicting the chemical reactivity to electrophilic and nucleophilic attack for major molecules, mapped on isosurface of total electron density at the value of $0.2|e| \text{ \AA}^{-3}$.

more reliable result in agreement with the implicit cluster method. For the reaction (2), the reaction energies were found to be negative by all the different methods, indicating the exothermicity of this reaction. In contrast to the reaction (1),

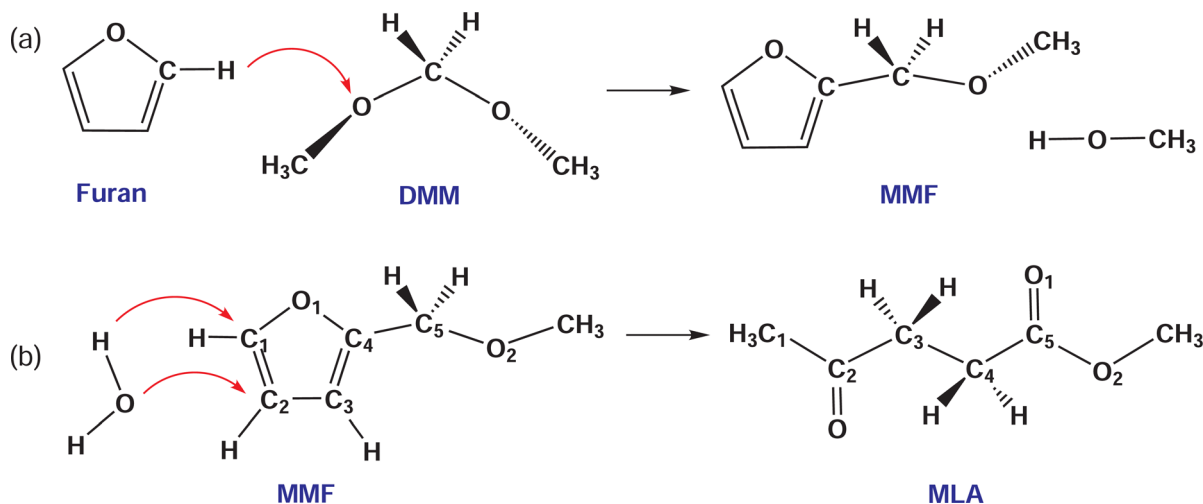
Table 3 Reaction energies for the chemical reactions described by eqn (1) and (2), calculated with PBE/DZP method using supercells in vacuum and explicit methanol solvent environments (Met-25 and Met-40) and with B3LYP/6-311+G* method using clusters in vacuum and implicit methanol solvent environments (unit: eV)

| | PBE/DZP | | | B3LYP/6-311+G* | |
|--------------|---------|--------|--------|----------------|-------|
| | Vac. | Met-25 | Met-40 | Vac. | Met. |
| Reaction (1) | 0.22 | -0.28 | -0.04 | 0.02 | -0.11 |
| Reaction (2) | -1.62 | -3.10 | -1.11 | -1.35 | -1.36 |

the methanol solvent barely affects the reaction energy for the B3LYP/6-311+G* cluster calculations. However, the reaction energy could be lowered by methanol solvent, except for the case of Met-40 model.

Then, we determined the activation barriers for these reactions by applying the NEB method. To do this, the reaction pathways were presumed previously. For the initial state (IS) and final state (FS) of the reactions, we prepared the bimolecular systems of furan + DMM, MMF + methanol and MMF + water molecules. In each bimolecular system, the two molecules were placed at a long distance over 2.5 Å with proper orientations according to the reactivity sites identified by Fukui functions (see Fig. 4) and the geometry optimization was performed. For the supercell modeling, the AIMD simulations were performed to equilibrate the systems at 300 K and subsequently atomic relaxations were performed. Also, the breaking chemical bonds of the reactant molecules and the newly formed chemical bonds of the product molecules were suggested by considering the Fukui functions. Scheme 6 shows the chemical reactions schematically with the movement direction





Scheme 2 Schematic processes for reactions of (a) furan + DMM to MMF + methanol and (b) MMF + water to MLA. Dashed arrows indicate a direction of atom movement to make a new chemical bond. Crosses denote a dissociation of chemical bond.

of the principal atoms of the reactants (red-coloured arrow). In the reaction (1), the hydrogen cation (proton) attached to the C1 atom adjacent to the O atom in furan is firstly dissociated and then reacted with the oxygen atom of DMM to create MMF, while forming a methanol molecule by bonding the proton with the CH₃-O- residue group, as depicted in Scheme 2(a). For the second reaction (2), the oxygen atom of water is reacted with the C2 atom of MMF and the hydrogen atoms of water are bonded to the C1 atom, leading to breaking and creation of several chemical bonds to form a MLA molecule, as depicted in Scheme 2(b).

With these expected reaction pathways, we performed the NEB simulations to evaluate the reaction barriers. Fig. 5 shows the energy profile for reaction of furan + DMM into MMF + methanol with the geometries of the bimolecular system corresponding to IS, transition state (TS) and FS, calculated

by using PBE/DZP method and the 30 Å supercell in vacuum. Through the geometry analysis during NEB run (see Fig. S5, ESI[†]), it was confirmed that as the furan molecule approached the DMM molecule, the H atom of C1-H bond in furan was firstly dissociated and bonded to the O2 atom of DMM, leading to the dissociation of DMM into CH₃-O1-CH₂- and CH₃-O2H (methanol). This indicates that in this reaction the furan and DMM act as Brønsted acid and base as they donate and receive the proton (H⁺), respectively. Then, the furan anion (C₄H₃O⁻) was combined with the remaining CH₃-O1-CH₂- group by forming a new chemical bond between C1 of furan and C2 of DMM to form a MMF molecule as expected before. The activation barrier for this reaction was calculated to be as high as 3.5 eV, as shown in Fig. 5.

For this reaction, we considered the methanol solvent effect explicitly using both the Met-25 and Met-40 models. The same reaction pathway was suggested. Fig. 6 shows the calculated energy profiles with the revealed supercell structures corresponding to IS, TS and FS (see Fig. S6, ESI[†]). Although some interacting methanol molecules existed around the reactant molecules, the reaction pathway and geometries were found not to be quite different from those in vacuum mentioned above. The activation barriers were also somewhat similar to that in vacuum as being about 3.3 and 3.7 eV in the Met-20 and Met-40 models, respectively. It should be noted that in these models the ISs were not the lowest energy states, which were found at the third and first NEB images for the Met-20 and Met-40 models, respectively. Also, the energy profiles resembled each other in overall shape as being mount-like, although being sharper in vacuum and wider bases in methanol solvents. This indicates that the methanol solvent barely affects the reaction pathway, and therefore only the results in vacuum will be considered hereafter.

Fig. 7 shows the energy profile for the second reaction (2) of MMF + water to MLA, calculated by using the PBE/DZP method and the 30 Å supercell in vacuum. The geometries of the

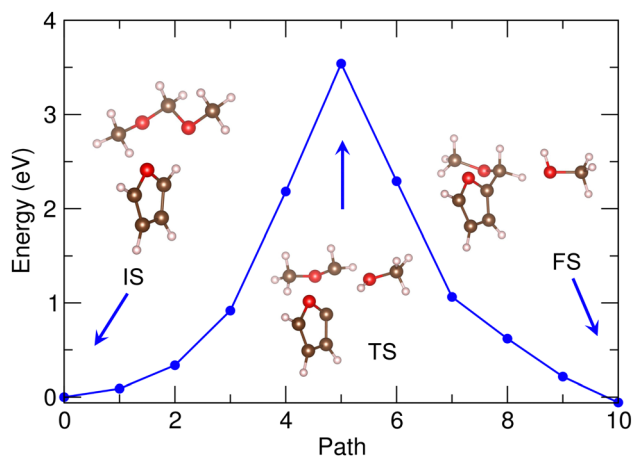


Fig. 5 Energy profile for reaction of furan + DMM to MMF + methanol calculated with PBE/DZP and 30 Å supercell in vacuum environment. Atomistic structures corresponding to the initial state (IS), transition state (TS) and final state (FS) are shown.



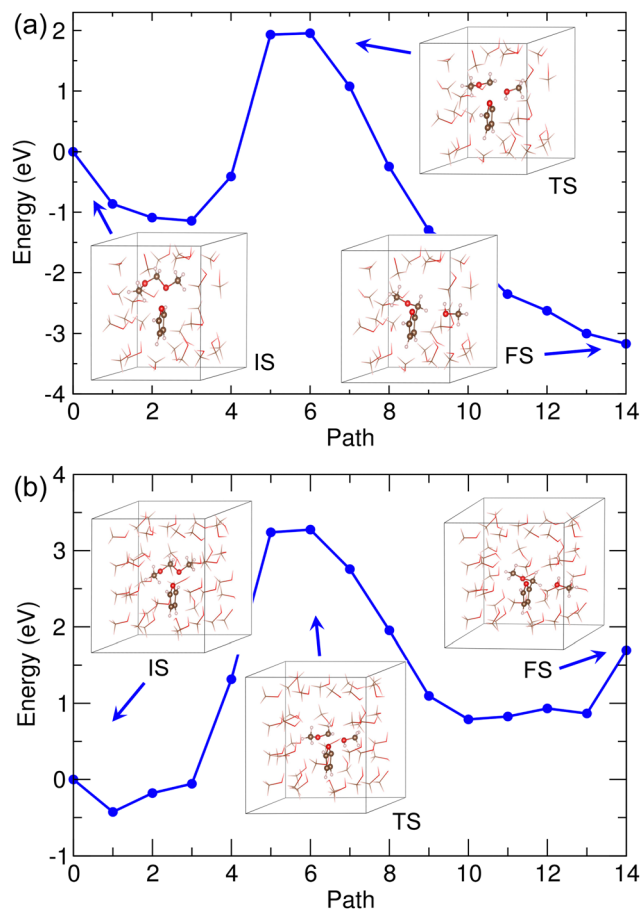


Fig. 6 Energy profile for reaction of furan + DMM to MMF + methanol calculated with (a) 12 Å supercell in 25 methanol and (b) 14 Å supercell in 40 methanol solvent environments. The solvent methanol molecules are depicted by stick and the reactant or product molecules are shown by ball-and-stick view.

molecules corresponding to IS, TS and FS are shown together (see Fig. S7, ESI[†]). In this reaction, water and MMF molecules

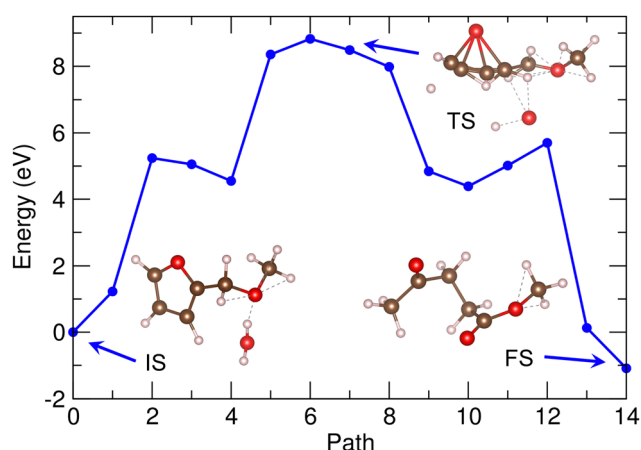


Fig. 7 Energy profile for reaction of MMF + water to MLA calculated with PBE/DZP method using the PBE functional and 30 Å supercell in vacuum environment, together with the molecular geometries corresponding to the initial state (IS), transition state (TS) and final state (FS).

could also act as Brønsted acid and base as they donate and receive two protons, respectively. When compared with the first reaction, many chemical bonds can be expected to be broken including the dissociation of furan heterocycle in MMF, while many chemical bonds can also be newly formed. Therefore, the activation energy might be higher. As shown in Fig. 7, the activation energy for this reaction was calculated to be 8.4 eV, being over twice higher than that for the first reaction. To make the reaction realistic, therefore, a certain catalyst is needed as the solid acidic resin catalyst of D008 was used in the real experiments.²⁰

Then, the B3LYP/6-311+G* method was applied to the cluster models in vacuum for determining the activation energies and reaction pathways for the two reactions. In these calculations, the number of NEB images was set to be 10. Fig. 8 shows the calculated energy profiles for the reactions (1) and (2). The real path distances were measured in the angstrom unit. We found that the reaction pathways and geometries of the molecules during the NEB runs were similar to those obtained by supercell calculations (see Fig. S8 and S9, ESI[†]). As shown in Fig. 8(a), the activation energy for the first

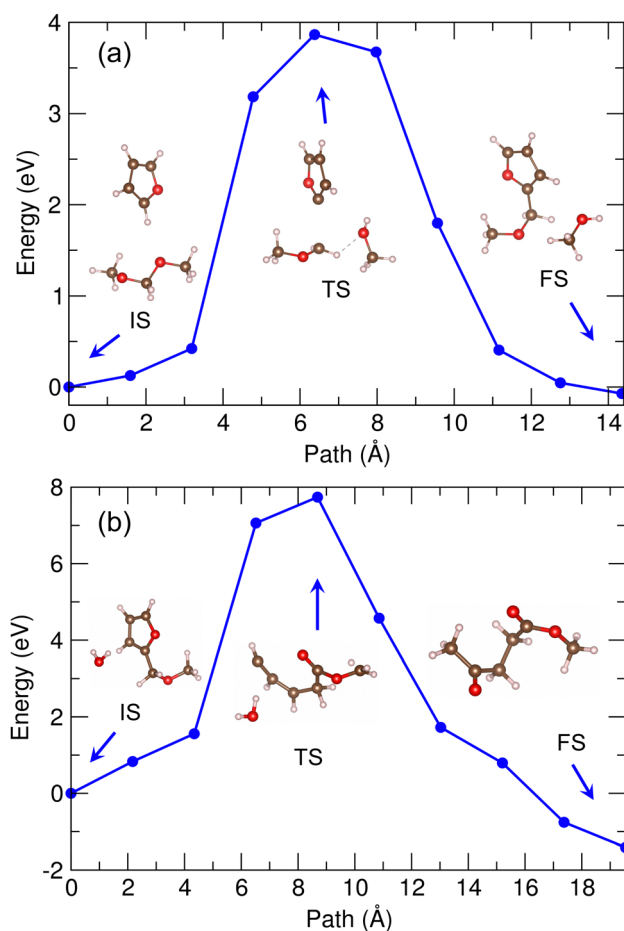


Fig. 8 Energy profile for reactions of (a) furan + DMM to MMF + methanol and (b) MMF + water to MLA calculated with B3LYP/6-311+G* cluster models in vacuum environment, together with geometries of molecules corresponding to IS, TS and FS.



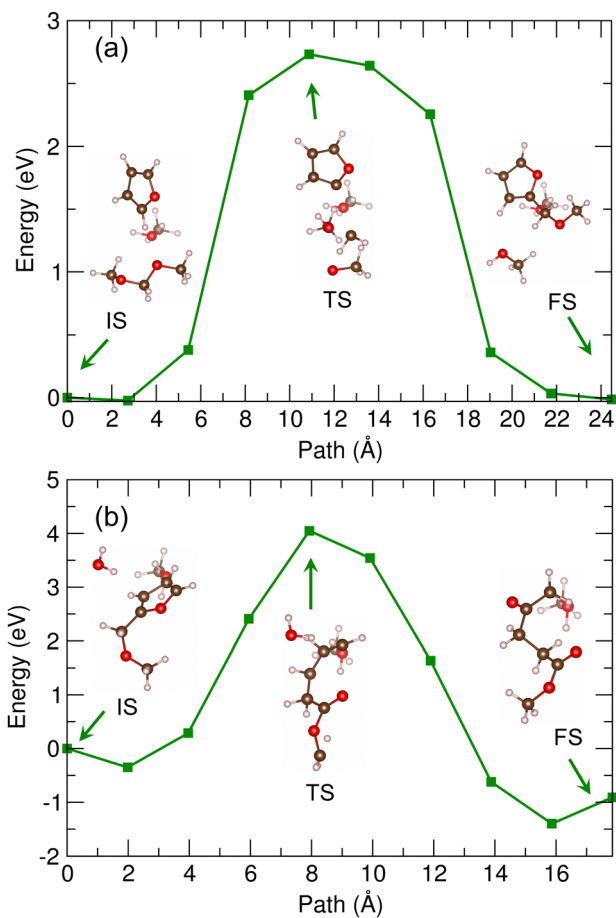


Fig. 9 Energy profile for reactions of (a) furan + DMM to MMF + methanol and (b) MMF + water to MLA with a protonated methanol molecule, calculated with B3LYP/6-311+G* cluster models in vacuum environment, together with geometries of molecules corresponding to IS, TS and FS.

reaction was calculated to be about 3.9 eV, which was slightly higher than that obtained with the Met-40 supercell calculation (3.8 eV). The mount-like shape of energy profile was also similar to those in the supercell calculation. For the second reaction, the activation energy was found to be about 7.9 eV, being similar to the case of the supercell calculation (see Fig. 8(b)). We note that the reason for such slight differences in activation energies might be slight differences in the optimized geometries of the molecules corresponding to IS, TS and FS. We performed the frequency analysis of TS. For the reaction (1), TS has only one imaginary frequency of -137 cm^{-1} , while for the reaction (2) TS exhibits an imaginary frequency of -230 cm^{-1} . To estimate the effect of different XC functional on the barrier height, we also applied the PBE/6-311+G* method to the NEB simulations for the reactions (1) and (2) (see Fig. S10, ESI[†]), confirming the almost agreement with those obtained with the DZP/PBE supercell as well as the B3LYP/6-311+G* method.

To consider the effect of solid acidic resin catalyst on the reaction barriers, we added a protonated methanol molecule into the original reaction systems⁶² and again performed NEB simulations. The protonated methanol molecule was located at the proper position between the reactant molecules with a

certain distance over 3 Å and fixed during the NEB simulations. Fig. 9 shows the calculated energy profiles for the reactions, together with the optimized geometries of molecules corresponding to IS, TS and FS (see Fig. S11 and S12 for all the NEB images, ESI[†]). The activation energies were found to be lowered as 2.8 and 4.1 eV for the reactions (1) and (2) respectively, compared with those obtained without a protonated methanol molecule. This indicates the positive role of the acidic resin catalyst in promoting the furan conversion into MLA.

4 Conclusions

In this work, we have studied the conversion of furan into methyl levulinate using *ab initio* calculations within the DFT framework. For modeling and simulation, we adopted two different ways of PAO-DZP basis sets with supercell modeling and 6-311+G* basis sets with cluster modeling. The methanol solvent effect was considered explicitly by including 25 and 40 methanol molecules in the supercells with lattice constants of 12 and 14 Å for the supercell modeling and implicitly by using the COSMO approach for the cluster modeling. The geometrical features of individual molecules of furan, DMM, MMF and MLA were analyzed with comparison between those by different methods and models. Through the analysis of the Fukui functions, we identifies the reactive sites in the individual molecules, being necessary for predicting the reaction pathways, and verify the Brønsted acid-base reaction fashions for these reactions. With the calculated DFT total energies, corrected by the zero-point and thermal energies for the cases of B3LYP/6-311+G* cluster calculations, we determined the reaction energies for the reactions of furan + DMM to MMF + methanol and MMF + water to MLA. It was revealed that the first reaction was endothermic in vacuum but became exothermic in methanol solvent, while the second reaction was exothermic in both vacuum and solvent environments. Using the predicted reaction pathways, we carried out the NEB simulations to clarify the real reaction pathways and determine the activation energies for these two reactions without and with a protonated methanol molecule. Our calculations provide the atomistic insight into conversion of biomass-derived furan to MLA used as fuel additive with the detailed geometries and frequencies of the intermediates.

Author contributions

Ryong-Wan Ham and Chol-Jun Yu developed the original project. Yun-Sim Kim and Chol-Jun Yu performed the calculations and drafted the first manuscript. Yong-Chol Pak, and Man-Sok O assisted with the post-processing of calculation results, and contributed to useful discussions. Chol-Jun Yu supervised the work. All authors reviewed the manuscript.

Conflicts of interest

There are no conflicts to declare.

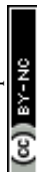


Acknowledgements

This work is supported as part of the basic research project “Design of New Energy Materials” (no. 2021-12) funded by the State Commission of Science and Technology, DPR Korea. Computations have been performed on the HP Blade System C7000 managed by Faculty of Materials Science, Kim Il Sung University.

References

- G. P. Robertson, S. K. Hamilton, B. L. Barham, B. E. Dale, R. C. Izaurralde, R. D. Jackson, D. A. Landis, S. M. Swinton, K. D. Thelen and J. M. Tiedje, *Science*, 2017, **356**, 6345.
- F. Qureshi, M. Yusuf, H. Kamyab, D.-V. N. Vo, S. Chelliapan, S.-W. Joo and Y. Vasseghian, *Renewable Sustainable Energy Rev.*, 2022, **168**, 112916.
- E. I. García-López, L. Palmisano and G. Marci, *Chem. Eng.*, 2023, **7**, 11.
- X. Cao, S. Sun and R. Sun, *RSC Adv.*, 2017, **7**, 48793–48805.
- S. D. Stefanidis, E. Heracleous, D. T. Patiaka, K. G. Kalogiannis, C. M. Michailof and A. A. Lappas, *Biomass Bioenergy*, 2015, **83**, 105–115.
- Y. Liu, Y. Chen, W. Guan, Y. Cao, F. Wang and Y. Zhang, *Catalysts*, 2023, **13**, 435.
- X. Li, Y. Wang, X. Xie, C. Huang and S. Yang, *RSC Adv.*, 2019, **9**, 9041–9048.
- S. Zhao, M. Cheng, J. Li, J. Tian and X. Wang, *Chem. Commun.*, 2011, **47**, 2176–2178.
- H. Zhao, J. E. Holladay, H. Brown and Z. C. Zhang, *Science*, 2007, **316**, 1597–1600.
- N. Kumari, T. Chhabra, S. Kumar and V. Krishnan, *Catal. Commun.*, 2022, **168**, 106467.
- K. C. Badgujar, L. D. Wilson and B. M. Bhanage, *Renewable Sustainable Energy Rev.*, 2019, **102**, 266–284.
- T. Flannelly, S. Dooley and J. J. Leahy, *Energy Fuels*, 2015, **29**, 7554–7565.
- M. S. Holm, S. Saravanamurugan and E. Taarning, *Science*, 2010, **328**, 602–605.
- A. Demolis, N. Essayem and F. Rataboul, *ACS Sustainable Chem. Eng.*, 2014, **2**, 1338–1352.
- J. Liu, X.-Q. Wang, B.-B. Yang, C.-L. Liu, C.-L. Xu and W.-S. Dong, *Renewable Energy*, 2018, **120**, 231–240.
- X. Hu, S. Jiang, L. Wu, S. Wang and C.-Z. Li, *Chem. Commun.*, 2017, **53**, 2938–2941.
- G. Xu, C. Chang, S. Fang and X. Ma, *Renewable Energy*, 2015, **78**, 583–589.
- H. Chen, H. Ruan, X. Lu, J. Fu, T. Langrish and X. Lu, *Chem. Eng. J.*, 2018, **333**, 434–442.
- G. Wang, Z. Zhang and L. Song, *Green Chem.*, 2014, **16**, 1436–1443.
- Z. Zhang, X. Hu, S. Zhang, Q. Liu, S. Hu, J. Xiang, Y. Wang and Y. Lu, *Fuel*, 2019, **237**, 263–275.
- Z. Chen, X. Ma, L. Xu, Y. Wang and J. Long, *Bioresour. Technol.*, 2018, **268**, 488–495.
- C. Chang, L. Deng and G. Xu, *Ind. Crops Prod.*, 2018, **117**, 197–204.
- J. Feng, J. Jiang, J. Xu, Z. Yang, K. Wang, Q. Guan and S. Chen, *Appl. Energy*, 2015, **154**, 520–527.
- X. Hu, Y. Song, L. Wu, M. Gholizadeh and C.-Z. Li, *ACS Sustainable Chem. Eng.*, 2013, **1**, 1593–1599.
- F. Müller, V. Hermann-Ene, I. Schmidpeter, T. Hammerschick and W. Vetter, *J. Agric. Food Chem.*, 2022, **70**, 12620–12628.
- S. Vaitheeswaran, S. K. Green, P. Dauenhauer and S. M. Auerbach, *ACS Catal.*, 2013, **3**, 2012–2019.
- X. Hu, S. Jiang, S. Kadarwati, D. H. Dong and C.-Z. Li, *RSC Adv.*, 2016, **6**, 40489–40501.
- H. Zhao, H. Gao, G. Yu, Q. Li and Z. Lei, *Fuel*, 2019, **241**, 704–714.
- Y. Dong, C. Dai and Z. Lei, *Fuel*, 2018, **216**, 503–512.
- B. Wang, X.-M. Liu, X.-N. Fu, Y.-L. Li, P.-X. Huang, Q. Zhang, W.-G. Li, L. Ma, F. Lai and P.-F. Wang, *Fuel*, 2018, **234**, 207–217.
- S. Yan, Y. Bu and L. Sun, *J. Mol. Struct.*, 2004, **671**, 161–172.
- A. Mellouki, J. Liévin and M. Herman, *Chem. Phys.*, 2001, **271**, 239–266.
- K. Sendt, G. B. Bacskay and J. C. Mackie, *J. Phys. Chem. A*, 2000, **104**, 1861–1875.
- E. Sánchez-García, A. Mardyukov, A. Tekin, R. Crespo-Otero, L. A. Montero, W. Sander and G. Jansen, *Chem. Phys.*, 2008, **343**, 168–185.
- V. Venkatesan, K. Sundararajan, K. Sankaran and K. S. Viswanathan, *Spectrochim. Acta, Part A*, 2002, **58**, 467–478.
- W. A. Kopp, L. C. Kröger, M. Döntgen, S. Jacobs, U. Burke, H. J. Curran, K. A. Heufer and K. Leonhard, *Combust. Flame*, 2018, **179**, 433–442.
- F. H. Vermeire, H.-H. Carstensen, O. Herbinet, F. Battin-Leclerc, G. B. Marin and K. M. Van Geem, *Combust. Flame*, 2018, **190**, 270–283.
- T. A. Halgren, *J. Am. Chem. Soc.*, 1992, **114**, 7827–7843.
- V. N. Emelyanenko, E. Altuntepe, C. Held, A. A. Pimerzin and S. P. Verevkin, *Thermochim. Acta*, 2018, **659**, 213–221.
- R. S. Assary, P. C. Redfern, J. R. Hammond, J. Greeley and L. A. Curtiss, *J. Phys. Chem. B*, 2010, **114**, 9002–9009.
- A. Klamt and G. Schürmann, *J. Chem. Soc., Perkin Trans. 2*, 1993, 799–805.
- CRC Handbook of Chemistry and Physics*, ed. D. R. Lide, C. R. C. Press, Boca Raton, FL, 2005, <https://www.hbcpnetbase.com>.
- E. Artacho, E. Anglada, O. Diéguez, J. D. Gale, A. García, J. Junquera, R. M. Martin, P. Ordejón, J. M. Pruneda, D. Sánchez-Portal and J. M. Soler, *J. Phys: Condens. Matter*, 2008, **20**, 064208.
- N. Troullier and J. L. Martins, *Phys. Rev. B: Condens. Matter Mater. Phys.*, 1991, **43**, 1993–2006.
- J. P. Perdew and A. Zunger, *Phys. Rev. B: Condens. Matter Mater. Phys.*, 1981, **23**, 5048.
- J. P. Perdew, K. Burke and M. Ernzerhof, *Phys. Rev. Lett.*, 1996, **77**, 3865.
- A. D. Becke, *Phys. Rev. B: Condens. Matter Mater. Phys.*, 1988, **38**, 3098–3100.



- 48 C. Lee, W. Yang and R. G. Parr, *Phys. Rev. B: Condens. Matter Mater. Phys.*, 1988, **37**, 785–789.
- 49 S. Grimme, *J. Comput. Chem.*, 2006, **27**, 1787–1799.
- 50 G. Henkelman, B. P. Uberuaga and H. Jónsson, *J. Chem. Phys.*, 2000, **113**, 9901–9904.
- 51 C.-J. Yu, Y.-H. Kye, U.-G. Jong, K.-C. Ri, S.-H. Choe, J.-S. Kim, S.-G. Ko, G.-I. Ryu and B. Kim, *ACS Appl. Mater. Interfaces*, 2020, **12**, 1858–1866.
- 52 Y.-S. Kim, C.-H. Ri, Y.-H. Kye, U.-G. Jong, X. Wang, Y. Zhang, X. Niu and C.-J. Yu, *J. Phys. Chem. C*, 2022, **126**, 3671–3680.
- 53 S.-A. Kim, Y.-C. Jong, M.-S. Kang and C.-J. Yu, *J. Mol. Model.*, 2022, **22**, 287.
- 54 M. Valiev, E. J. Bylaska, N. Govind, K. Kowalski, T. P. Straatsma, H. J. J. van Dam, D. Wang, J. Nieplocha, E. Apra, T. L. Windus and W. A. de Jong, *Comput. Phys. Commun.*, 2010, **181**, 1477–1489.
- 55 A. D. Becke, *J. Chem. Phys.*, 1993, **98**, 5648–5652.
- 56 Y. Zhao and D. G. Truhlar, *Theor. Chem. Acc.*, 2008, **120**, 215–241.
- 57 A. Klamt, V. Jonas, T. Brüger and J. C. W. Lohrenz, *J. Phys. Chem. A*, 1998, **102**, 5074–5085.
- 58 L. A. Montero, R. Gonzalez-Jonte, L. A. Diaz and J. R. Alvarez-Idaboy, *J. Phys. Chem.*, 1994, **98**, 5607.
- 59 A. Jiao, H. Zhang, J. Liu and X. Jiang, *Combust. Flame*, 2018, **196**, 377–385.
- 60 R. Salcedo, A. Martínez and L. E. Sansores, *Tetrahedron*, 2001, **57**, 8759–8765.
- 61 N. Gavrilov, S. Salzmann and C. M. Marian, *Chem. Phys.*, 2008, **349**, 269–277.
- 62 N. Nikbin, S. Caratzoulas and D. G. Vlachos, *ChemSusChem*, 2013, **6**, 2066–2068.

